

Article

Spanwise-Discontinuous Grooves for Separation Delay and Drag Reduction of Bodies with Vortex Shedding

Elena Pasqualetto , Gianmarco Lunghi , Alessandro Mariotti *  and Maria Vittoria Salvetti 

Dipartimento di Ingegneria Civile e Industriale, Università di Pisa, Largo Lazzarino 2, 56122 Pisa, Italy; elena.pasqualetto@phd.unipi.it (E.P.); gianmarco.lunghi@phd.unipi.it (G.L.); mv.salvetti@ing.unipi.it (M.V.S.)

* Correspondence: alessandro.mariotti@for.unipi.it; Tel.: +39-050-2217260

Abstract: Suitably shaped grooves, placed transverse to the flow, can delay flow separation over curved surfaces. When grooves are fully extruded in the spanwise direction, they may reduce the drag of boat-tailed bodies with vortex shedding, but with the drawback of increasing the spanwise correlation of the vortex shedding. We investigate herein the effect of spanwise-discontinuous grooves through Large Eddy Simulations. A systematic analysis is carried out on the effect of the number, N , of grooves that are present for N equally long portions of the total spanwise length of the boat-tail. Discontinuous grooves further reduce the drag compared with the full-spanwise-extruded groove. Increasing N produces an improvement of the flow-control-device performance, whose maximum value is reached for $N = 3$, corresponding to a spanwise extension of the groove roughly equal to the body crossflow dimension. Above this value, no further improvements are found. The maximum drag reduction is equal to 25.7% of the drag of the boat-tail without grooves and to 17.7% of the one of the boat-tail with the full-spanwise-extruded groove. The lowest drag value occurs for the least correlated vortex-shedding in the spanwise direction. The reduction in the correlation is mainly related to a flow separation line that is less regular in the spanwise direction.



Citation: Pasqualetto, E.; Lunghi, G.; Mariotti, A.; Salvetti, M.V. Spanwise-Discontinuous Grooves for Separation Delay and Drag Reduction of Bodies with Vortex Shedding. *Fluids* **2022**, *7*, 121. <https://doi.org/10.3390/fluids7040121>

Academic Editor: Amir Teimourian

Received: 13 January 2022

Accepted: 20 March 2022

Published: 23 March 2022

Publisher's Note: MDPI stays neutral with regard to jurisdictional claims in published maps and institutional affiliations.



Copyright: © 2022 by the authors. Licensee MDPI, Basel, Switzerland. This article is an open access article distributed under the terms and conditions of the Creative Commons Attribution (CC BY) license (<https://creativecommons.org/licenses/by/4.0/>).

Keywords: spanwise-discontinuous grooves; flow-separation delay; drag reduction; boat-tailed bluff bodies

1. Introduction

Drag reduction in bluff bodies is very important in many engineering applications and this can often be obtained through the delay of boundary layer separation (see, e.g., [1,2] and the references therein). In the present paper, we aim at reducing the drag of a boat-tailed bluff body with vortex shedding by introducing spanwise-discontinuous grooves in the boat-tail lateral surface as a passive flow-control device. The boat-tail is itself a strategy for bluff-body drag reduction consisting in a gradual decrease in the cross-section length of the body upstream of the base, d . For a given diameter of the main body, D , the recovery of pressure increases by decreasing d/D ; but the boat-tail is advantageous in case the flow does not separate almost up to the rear base [3,4]. The introduction of suitably shaped grooves is aimed at delaying the separation of the boundary layer thanks to the generation of local steady flow recirculations, improving, thus, the boat-tail drag-reducing performance.

Rectangular grooves may lead to a flow-separation delay for boat-tailed axisymmetric bodies by [5,6] and for a backward-facing ramp by [7,8]. A series of cavities were also introduced over the diverging curved wall in [9,10] to delay flow separation through the so-called “roller bearing” mechanism, i.e., the formation of a succession of recirculation regions adjacent to the solid surface. Dolphin-skin-inspired sinusoidal and rectangular grooves were successfully used in [11,12] to boundary-layer separation delay over a flat plate in an adverse pressure gradient. More recently, the effectiveness of small and suitably-shaped contoured grooves, placed transverse to the flow, is proved in [13–17] in delaying

boundary-layer separation in adverse pressure gradient for different internal and external flows thanks to the generation of local steady flow recirculations. In particular, contoured transverse grooves were successfully introduced in the diverging walls of plane diffusers to avoid or, at least, delay flow separation and, thus, to improve pressure recovery in different operating conditions [13–15]. In [16], transverse contoured grooves were introduced in the lateral surface of axisymmetric boat-tailed bluff bodies with different degrees of flow separations occurring over the boat-tail. Experiments and LES simulations were used to optimize the groove parameters and analyze the physical mechanism leading to the flow-separation delay and to the aerodynamic-drag reduction. Finally, the grooves were also extruded in the full spanwise direction of a boat-tailed bluff body with vortex shedding [17], i.e., spanwise-extruded grooves in the following of the paper. The large fluctuations of pressure and velocity occurring along the boat-tail lateral surface due to the alternate vortex shedding make it more challenging to obtain a steady recirculation embedded in the groove region. However, also for this body, groove introduction led to the formation of steady recirculations and, thus, to a reduction in both the wake width and the boat-tail drag.

From a physical viewpoint, the local steady recirculations within the grooves produce a local relaxation of the no-slip boundary condition, which reduces energy losses in the boundary layer, delaying, thus, its separation [16]. The optimal grooves identified in [16,17] should have: (i) a depth smaller than the thickness of the upstream boundary layer and (ii) no rear corners in their shape. These two characteristics are fundamental to obtain a steady passive recirculation and to avoid the presence of self-sustained cavity oscillations [16,18–23]. Indeed, blowing and suction or a similar active control is needed to assure the steadiness of the vortices forming in the cavity region that is much larger than the thickness of the incoming boundary layer (see, e.g., [24–26]) and a significant reduction in the velocity and pressure fluctuations can be obtained by changing the rear wall of a rectangular cavity to a rounded or slanted ramp (see, e.g., [19,27–31]).

The present work is motivated by the observation that the introduction of the spanwise-extruded groove in [17] significantly increases the vortex-shedding correlation in the spanwise direction. This is due to the formation of a straighter flow separation line for the presence of the groove [17]. Spanwise-discontinuous grooves were firstly proposed in the preliminary study in [32], where two spanwise-discontinuous grooves were introduced instead of the spanwise-extruded one, showing almost the same flow-separation delay performance with a large reduction in the vortex-shedding correlation in the spanwise direction. Indeed, a less-straight separation line was found leading to wavy vortical structures in the near wake. The present work further extends the idea of [32] by a numerical systematic analysis of the performance in reducing drag and vortex-shedding correlation as a function of the number of grooves placed along the spanwise direction, i.e., of the groove length in this direction. Variational Multi-Scale Large-Eddy Simulations (VMS-LES) have been carried out through a proprietary code, based on a mixed finite-volume/finite-element method, applicable to unstructured grids for space discretization. The code has been widely used to simulate bluff-body flows in the past (see, e.g., [16,17,33]). A key feature of VMS-LES [34] is that the SGS model is only added to the smallest resolved scales. This is aimed at reducing the excessive dissipation introduced by non-dynamic eddy-viscosity SGS models also on the large scales and this has been shown to generally improve the behavior of such models, such as, for instance, for the Smagorinsky model in boundary layers [35]. Clearly, the VMS approach is a possible choice among several strategies proposed in the literature to improve the behavior of eddy-viscosity SGS models, such as, for instance, the dynamic procedure [36] or the combination with scale-similarity terms [37]. The VMS approach is particularly attractive for variational numerical methods and unstructured grids, because it is easily incorporated in such formulations [35,38] and the additional computational costs with respect to classical LES are very low. An alternative approach could be the Lagrangian one, as suggested in [39,40]. Results of the VMS-LES are compared with the ones obtained with the same code in [17] for the spanwise-extruded groove having the same geometrical parameters and location.

2. Geometry Definition

The geometry of the boat-tailed bluff body considered herein is the same as in [17]. The streamwise section of the body, consisting of a 3:1 elliptical forebody followed by a rectangular main part and a circular-arc boat-tail, is extruded in the spanwise direction for a length equal to the total streamwise dimension of the body, L (see Figure 1, where the reference system is also shown). The body is considered infinite in the spanwise direction and, thus, periodic boundary conditions are applied in that direction to the portion previously described. The ratio between the streamwise length of the body, L , and its cross-flow dimension, D , is $L/D = 5.71$. The boat-tail streamwise length is equal to $D/2$ and its base ratio is $d/D = 0.791$.

N grooves are extruded in spanwise direction for N equally-long portions of the total spanwise length of the boat-tail, each one of $m = L/(2N)$ (see Figure 1 for $N = 3$). In this paper, N ranges from $N = 1$ to $N = 4$, i.e., from one spanwise-discontinuous groove (1 DG) to four spanwise-discontinuous grooves (4 DG). The groove cross-section is sketched in Figure 2: it has an upstream part with a sharp edge and a semi-elliptical shape and a rear part with a spline tangent to the lateral surface of the boat-tail. Position and dimensions of the groove are the optimal ones found in [17] for a spanwise-extruded groove. In particular, the distance of the sharp edge of the groove from the most upstream point of the boat-tail is $s/D = 0.065$, the total length of the groove is $b/D = 0.13$, its depth $h/D = 0.024$ and the length of the semi-ellipse x-axis $a/D = 0.016$.

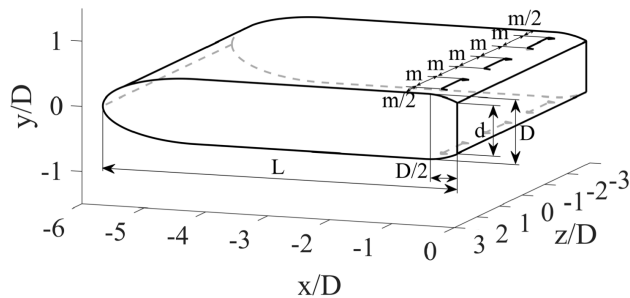


Figure 1. Sketch of the body geometry.

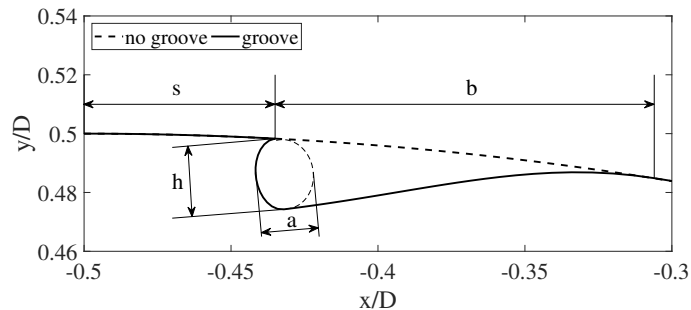


Figure 2. Groove geometry and main parameters.

3. Numerical Methodology and Simulation Set-Up

The LES equations are:

$$\begin{cases} \frac{\partial \bar{\rho}}{\partial t} + \frac{\partial \bar{\rho} \bar{u}_j}{\partial x_j} = 0 \\ \frac{\partial \bar{\rho} \bar{u}_i}{\partial t} + \frac{\partial \bar{\rho} \bar{u}_i \bar{u}_j}{\partial x_j} = -\frac{\partial \bar{p}}{\partial x_i} - \frac{\partial}{\partial x_j} (\mu \tilde{P}_{ij}) - \frac{\partial M_{ij}}{\partial x_j} \\ \frac{\partial \bar{\rho} \bar{e}}{\partial t} + \frac{\partial [(\bar{\rho} \bar{e} + \bar{p}) \bar{u}_j]}{\partial x_j} = \frac{\partial (\bar{u}_j \mu \tilde{P}_{ij})}{\partial x_j} - \frac{\partial \tilde{q}_{ij}}{\partial x_j} + \frac{\partial H_j}{\partial x_j} \end{cases} \quad (1)$$

in which μ , p , e , and u_i are viscous, pressure, total energy, and velocity components in the i direction. The symbol \sim denotes the Favre filter, while the overbar is the grid filter:

$$\tilde{f} = \frac{\overline{\rho}\tilde{f}}{\overline{\rho}} \quad (2)$$

The tensor \tilde{P}_{ij} writes as:

$$\tilde{P}_{ij} = -\frac{2}{3}\tilde{S}_{kk}\delta_{ij} + 2\tilde{S}_{ij} \quad (3)$$

\tilde{S}_{ij} being the resolved strain tensor. Some subgrid scale terms are discarded under the assumption that low compressibility effects are present in the SGS fluctuations and that heat transfer and temperature gradients are moderate [41]. Therefore, the terms to be modeled are the classical SGS stress tensor:

$$M_{ij} = \overline{\rho u_i u_j} - \overline{\rho} \tilde{u}_i \tilde{u}_j \quad (4)$$

and

$$H_i = \tilde{u}_i(\overline{\rho e} - \overline{p}) - \overline{u_j(\rho e + p)} \quad (5)$$

As for the SGS tensor, the isotropic heat can be neglected under the previous assumptions, while its deviatoric part is expressed by the Smagorinsky model [41,42]:

$$M_{ij} = -\overline{\rho}(C_S \Delta_S)^2 |\tilde{S}| \tilde{P}_{ij} = -\mu_{SGS} \tilde{P}_{ij} \quad (6)$$

where Δ_S is the filter width ad $C_S = 0.1$, which is a value widely adopted in the literature. Finally, $|\tilde{S}| = \sqrt{2\tilde{S}_{ij}\tilde{S}_{ij}}$. The term H in the energy equation is modelled through a constant Prandtl number as follows:

$$H_i = C_P \frac{\mu_{SGS}}{Pr_{SGS}} \frac{\partial T}{\partial x_i} \quad (7)$$

where C_P is the constant pressure specific heat and Pr_{SGS} is set equal to 0.76.

Variational Multi-Scale Large-Eddy Simulations (VMS-LES) of the considered configurations are performed through AERO, a compressible flow solver that has already been successfully used for the simulation of this kind of problems (see, e.g., [16,17,33]). The governing equations are discretized in space through a mixed finite-element/finite-volume method applicable to unstructured grids. The resulting scheme is second-order accurate and is stabilized through a very low numerical diffusion built with a sixth-order spatial derivative, weighted by the 5th power of local mesh size and by a tunable coefficient. The impact of this stabilizing term has been evaluated as very low (see, e.g., [43,44]). Thanks to the VMS formulation, a splitting is introduced between the Large Resolved Scales (LRS), i.e., those resolved on a virtual coarser grid (roughly of size $2\Delta x$, Δx being the local grid resolution), and the small resolved ones (SRS, of size Δx). The scale separation is obtained through a projector operator in the LRS space, which is based on spatial average on macro-cells, obtained through agglomeration of the finite-volume cells associated to the used grid [38]. Finally, we adopt herein the so called small-small formulation, i.e., the SGS term is computed as a function of the SRS only. Additional details on the methodology can be found in [43,44].

The same domain and boundary conditions as in [17] are used. The rectangular domain has a cross-section of $5.71D \times 150D$ and a length of $50D$, as shown in Figure 3. The blockage factor is about 0.66%. Characteristic-based boundary conditions are set at the inlet, outlet, and upper and lower surfaces of the domain (see, e.g., [43]), periodic conditions are used in the spanwise direction, while no slip is imposed along the surface of the body. An unstructured grid with approximately 2×10^6 nodes is used to discretize the computational domain ([32]). The grid is particularly refined near the body surface, where the wall y^+ is lower than 1, and in the near wake.

Simulations are performed for laminar free-stream conditions at a Reynolds number $Re = u_\infty D / \nu = 9.6 \times 10^4$. At the inflow, a time-constant and uniform velocity is assumed and the free-stream Mach number is equal to 0.1 to make compressibility effects negligible. A second-order upwind scheme preconditioned for the low Mach regime is used for the

space discretization (see, e.g., [43]). An implicit second-order time advancing scheme is adopted. The dimensionless time step is $\Delta t(u/D) = 1.86 \cdot 10^{-4}$ that is more than two orders of magnitude smaller than the vortex-shedding period in the wake. This time step corresponds to a CFL, defined in each cell as $\text{CFL} = \Delta t(u/\Delta x)$, with a maximum value at each time step of approximately 20, that is well below the stability limits of the chosen implicit scheme for time advancing. Flow statistics shown in the paper are evaluated by neglecting an initial numerical transient and then computing than on a time interval of $160t(u/D)$ that corresponds to more than 50 vortex-shedding cycles.

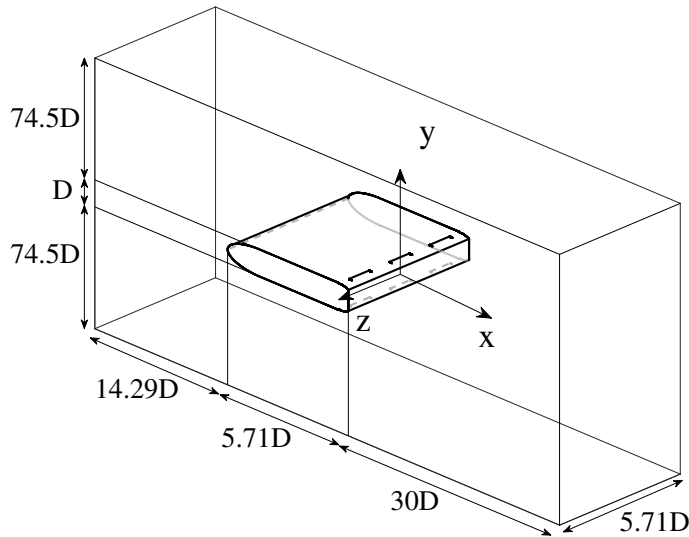


Figure 3. Sketch of the computational domain (not in scale).

4. Results and Discussion

The boat-tail mean-drag coefficients, $C_{D,tot}^{bt}$, for the four considered spanwise-discontinuous grooves are summarized in Table 1 and compared with the results for the boat-tail without grooves and for the optimal spanwise-extruded groove in [17]. Drag coefficients are defined as:

$$C_D^i = \frac{D^i}{\frac{1}{2}\rho u_\infty L D} \quad (8)$$

where D^i is the drag of the considered portion of the body (e.g., boat-tail lateral surface, boat-tail base). Moreover, the value of the pressure coefficient averaged in time and on the base of the boat-tail $\bar{C}_{p,base}$ is reported, evaluated as:

$$\bar{C}_{p,base} = \frac{\int_{base} \bar{C}_p dy dz}{Ld} \quad (9)$$

with the time-averaged pressure coefficient is defined as $\bar{C}_p = (p - p_\infty)/(\frac{1}{2}\rho_\infty u_\infty^2)$, being \bar{p} the time-averaged local pressure, p_∞ and ρ_∞ the free-stream pressure and density of the air, respectively.

For all the four values of N , the introduction of spanwise-discontinuous grooves allows a further reduction in the total boat-tail mean drag coefficient compared with the extruded groove. A maximum reduction in $C_{D,tot}^{bt}$ is obtained by using 3 DG, i.e., with $N = 3$. For this configuration, a reduction of 25.7% is found in comparison with the boat-tail without grooves and of 17.7% compared with the case of the spanwise-extruded groove. The drag reduction is almost completely due to a decrease in the pressure contribution to the drag, $C_{D,p}^{bt}$, whereas the boat-tail mean viscous drag coefficient, $C_{D,v}^{bt}$, does not significantly change among the investigated configurations. In particular, the reduction in the boat-tail pressure drag coefficient is mainly related to an increase in the mean pressures acting on the base of the boat-tail, $\bar{C}_{p,base}$, with a consequent decrease in the base contribution to the

total drag, $C_{D,p}^{base}$. On the other hand, the contribution of the boat-tail lateral surface does not significantly change among the considered cases and it is equal to the extruded-groove one in [17].

Table 1. Pressure and viscous contributions to drag coefficient and average base pressure coefficient compared to the boat-tail without and with spanwise-extruded grooves from [17].

	$C_{D,tot}^{bt}$	$C_{D,p}^{bt}$	$C_{D,v}^{bt}$	$C_{D,p}^{ls}$	$C_{D,p}^{base}$	$\bar{C}_{p,base}$
1 DG	0.3669	0.3664	0.0005	0.0865	0.2799	-0.354
2 DG	0.3404	0.3399	0.0005	0.0833	0.2566	-0.325
3 DG	0.3113	0.3108	0.0005	0.0807	0.2300	-0.291
4 DG	0.3470	0.3465	0.0005	0.0843	0.2623	-0.332
no groove	0.4191	0.4183	0.0008	0.0853	0.3330	-0.421
extruded groove	0.3783	0.3778	0.0005	0.0835	0.2942	-0.372

The time history of the drag coefficient is shown in Figure 4. It is clearly evident how the introduction of grooves reduces the drag coefficient. This reduction is larger by introducing spanwise-discontinuous grooves. The standard deviation of the drag coefficient is reported in Table 2. Consistently with the previous observations, the introduction of one or more spanwise grooves decreases the C_D standard deviation. The minimum is reached for $N = 3$, for which the maximum mean drag reduction is obtained.

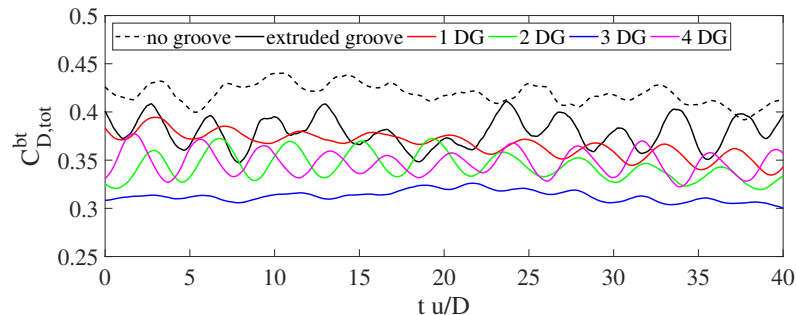


Figure 4. Time history of the drag coefficient.

Three streamwise sections are considered for the analysis of the pressure and velocity fields, corresponding to the center of the boat-tail portion between two grooves, to the groove edge and to its central section, respectively. As an example, a sketch of the three considered streamwise sections for the case with $N = 1$ is shown in Figure 5 (left panel), together with the relative mean velocity fields and mean flow streamlines (right panel). A recirculation region is present inside the groove region, as for the spanwise-extruded grooves in [17]. This recirculation causes a slip velocity of the order of $0.25 u_\infty$ to be present over the groove at the same coordinate characterized by a no-slip boundary condition in the boat-tail without the groove. This reduces the energy losses in the boundary layer and leads to a stronger resistance to separation of the boundary layer developing downstream of the groove.

We analyze now how the separation point location varies in time during the vortex-shedding cycle for the case $N = 1$. The vorticity fields and the instantaneous streamlines in the plane $z/D = 0$ are shown in Figure 6 for 6 equally spaced time intervals during a vortex shedding cycle of period τ , being $\tau = 1/St = 1/0.323$. In particular, Figure 6a shows the vorticity field around the boat-tail lateral surface and in the near wake, whereas Figure 6b shows the instantaneous streamlines over the lateral surface of the boat-tail. The flow separation points may be identified for each time instant, and its location is illustrated in Figure 7, for the boat-tail upper surface. When the vortex is forming on the upper side,

the upper boundary-layer separation point moves downstream up to $x_{sep}/D = -0.22$, whereas it moves upstream up to $x_{sep}/D = -0.29$ when the vortex is forming on the other side. The range of oscillation of the location of the separation point for all the analyzed cases are reported in Table 2.

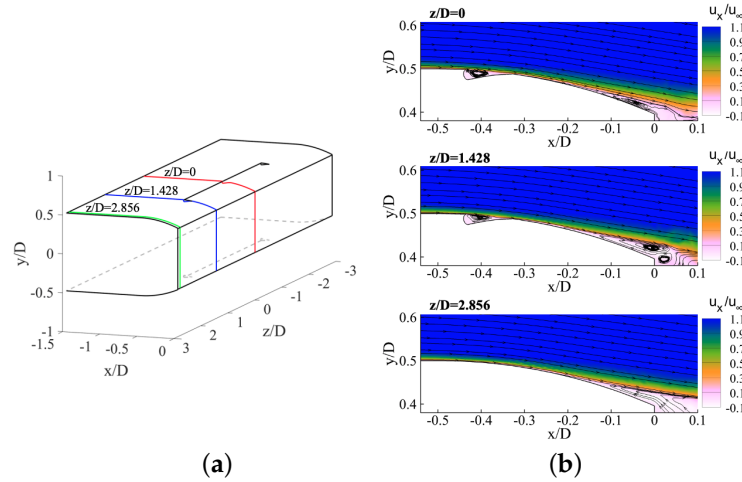


Figure 5. (a) Sketch of the considered streamwise sections and (b) mean velocity field and streamlines at sections $z/D = 0$, $z/D = 1.428$, $z/D = 2.856$ (from top to bottom) for the case $N = 1$.

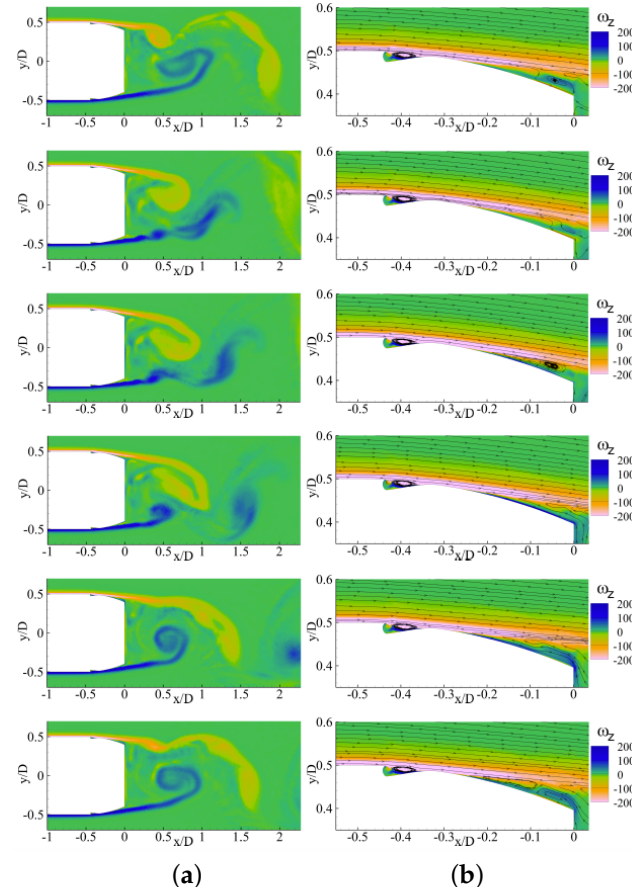


Figure 6. (a) Vorticity field during the vortex-shedding cycle and (b) on the lateral surface of the boat-tail $y/D > 0$. Time instants (from top to bottom): $t/\tau = 0$, $t/\tau = 0.17$, $t/\tau = 0.33$, $t/\tau = 0.5$, $t/\tau = 0.67$ and $t/\tau = 0.83$, τ being the vortex-shedding period.

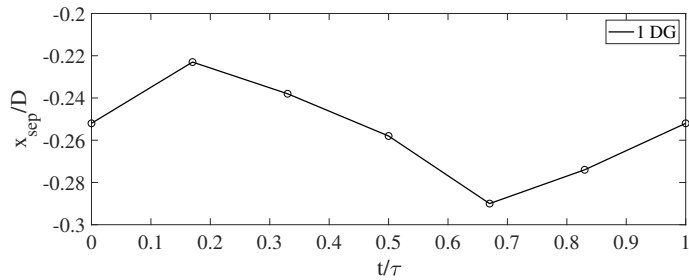


Figure 7. Time behavior of the separation point on the lateral side of the boat-tail for $y/D > 0$ during the vortex-shedding cycle.

In Figure 8 the spanwise distributions of the values of (x_{sep}, y_{sep}) averaged in time during the vortex-shedding cycle, indicated with $(\bar{x}_{sep}, \bar{y}_{sep})$, are shown with continuous lines. Moreover, the spanwise distributions of the minimum and maximum values of (x_{sep}, y_{sep}) during the vortex-shedding cycle are reported with dashed lines.

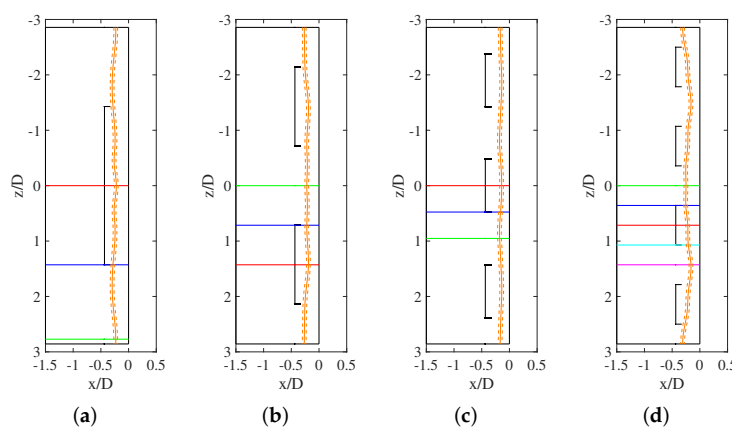


Figure 8. Spanwise distributions of $(\bar{x}_{sep}, \bar{y}_{sep})$ (orange continuous line) and of the minimum and maximum values of (x_{sep}, y_{sep}) during the vortex-shedding cycle (orange dashed lines). Cases: (a) $N = 1$, (b) $N = 2$, (c) $N = 3$, and (d) $N = 4$. The cross-section considered to evaluate the pressure coefficient distributions in Figure 9 are also sketched.

Table 2. Mean separation point and its maximum variation during a vortex-shedding cycle, vortex-shedding Strouhal number and the standard deviation of the drag coefficients. The results for the boat-tail without the groove and for the extruded groove are from [17].

	$\langle x_{sep} \rangle / D$	$\langle y_{sep} \rangle / D$	x_{sep}^{\min} / D	x_{sep}^{\max} / D	St	$\sigma(C_D)$
1 DG	-0.256	0.476	-0.331	-0.188	0.323	0.0153
2 DG	-0.226	0.470	-0.299	-0.158	0.333	0.0148
3 DG	-0.158	0.452	-0.215	-0.108	0.342	0.0064
4 DG	-0.233	0.471	-0.345	-0.128	0.332	0.0131
no groove	-0.325	0.487	-0.360	-0.293	0.304	0.0133
extruded groove	-0.269	0.478	-0.304	-0.237	0.319	0.0168

The coordinates of the separation point averaged in time and also in the spanwise direction ($\langle x_{sep} \rangle, \langle y_{sep} \rangle$) and the most upstream and downstream positions of the separation point, x_{sep}^{\max} and x_{sep}^{\min} , respectively, are summarized in Table 2. For all the considered values of N , $(\langle x_{sep} \rangle, \langle y_{sep} \rangle)$ is significantly moved downstream compared with the case of the spanwise-extruded groove. In the spanwise direction, the mean separation line is no more straight, but exhibits a number of waves equal to N for $N \leq 3$ (see Figure 8a–c).

The delay of the separation point is more evident downstream of the portions of the boat-tail where the grooves are placed, but it is moved downstream also between them. The physical mechanism leading to the delay of boundary-layer separation holds also for the spanwise-discontinuous grooves, i.e., the relaxation of the no-slip condition on the streamlines bounding the recirculation inside the groove produces a boundary layer downstream of the groove which has more momentum and better resists the adverse pressure gradient. Additionally, in the region between two grooves, the boundary layer separates more downstream than for the boat-tail without the grooves, although the effect is lower. It should be noted that for $N = 4$ (Figure 8d) the behavior of the separation point in the spanwise direction is similar to the one found for the case $N = 2$ (compare Figure 8d with Figure 8b). The best performance of the flow control device in terms of drag reduction and separation delay is obtained for $N = 3$. Results for $N = 2$ and $N = 4$ are almost similar. The separation delay produces, also, a narrowing of the wake and, in turn, an increase in the non-dimensional vortex shedding frequency, evaluated in terms of Strouhal number, $St = f \cdot D / u_\infty$, as previously found also in [17,45,46]. These results, which match the typical values identified in [47] for similar bluff-body shapes, are reported in Table 2. It is evident how the Strouhal numbers for DG cases are higher than the ones found in [17] for the plain boat-tail and the boat-tail with the spanwise-extruded groove because the wake width is smaller. Consistently with the previous analyses, the maximum value of the vortex shedding frequency is obtained for the narrowest wake of the case $N = 3$.

Flow separation delay has a significant effect on the curvature of the mean streamlines and this, in turn, affects the pressure distribution on the body. The time-averaged distributions of the pressure coefficient are shown in Figure 9. The left-hand part of Figure 9a–d shows the C_p values on the last portion of the lateral surface of the body, along which at $x/D = -0.5$ the boat-tail starts; the right-hand part of the same figures reports the C_p behavior along the base of the boat-tail, starting from its outer border. Four vertical lines and a sketch indicating the position of the groove are also shown. For each case, three streamwise sections are considered, viz. one placed at the center of the groove (red line), one at the border of the groove (blue), and the last one between two grooves (green). The black dashed line represents the case without groove, while the black continuous line represents the spanwise-extruded groove placed in the same position from [17]. For all the spanwise-discontinuous grooves, the larger streamline curvature leads to higher suction on the boat-tail lateral surface and, in turn, to the previously-observed increased contribution of the lateral surface on the total pressure drag. On the other hand, the discontinuous groove is characterized by a further delay of flow separation point for all the considered spanwise sections and by a stronger pressure recovery in the last part of the boat-tail that leads to higher pressure values on the base of the boat-tail. The stronger effect is again found for the 3 DG case (Figure 9c). It is worth mentioning that small differences are found between the streamwise sections in the middle of the groove (red line) and the one between two grooves (green line), confirming that also the latter sections benefit from the presence of the spanwise-discontinuous grooves.

As for the dynamics of the near wake, at the Reynolds number of the present investigation, an alternate shedding of vortical structures is present downstream of the body. These vortical structures are shown in Figure 10 through the isocontours of the vortex indicator λ_2 ([48]), which is able to well describe the dynamics of coherent vortical structures in unsteady flows (see, e.g., [17,45]). Following the λ_2 -criterion, a vortex may be identified by a connected fluid region in which the second largest eigenvalue of the 3×3 tensor Q is negative, i.e., where $\lambda_2 < 0$. The tensor Q is symmetric and defined as $Q = \Omega \cdot \Omega + E \cdot E$, where Ω and E are the antisymmetric and the symmetric part of the velocity gradient, respectively. Wavy vortical structures are present in the near wake when spanwise-discontinuous grooves are introduced in the boat-tail lateral surface. N wavies in the spanwise direction are present for $N \leq 3$ while the case $N = 4$ has a similar behavior to $N = 2$, as previously found for the separation line in Figure 10. These vortices are, thus, less regular in spanwise direction than the straight-vortices found for the spanwise-extruded

grooves in [17]. The reduction in the vortex-shedding correlation in the spanwise direction is generally desirable in practical applications.

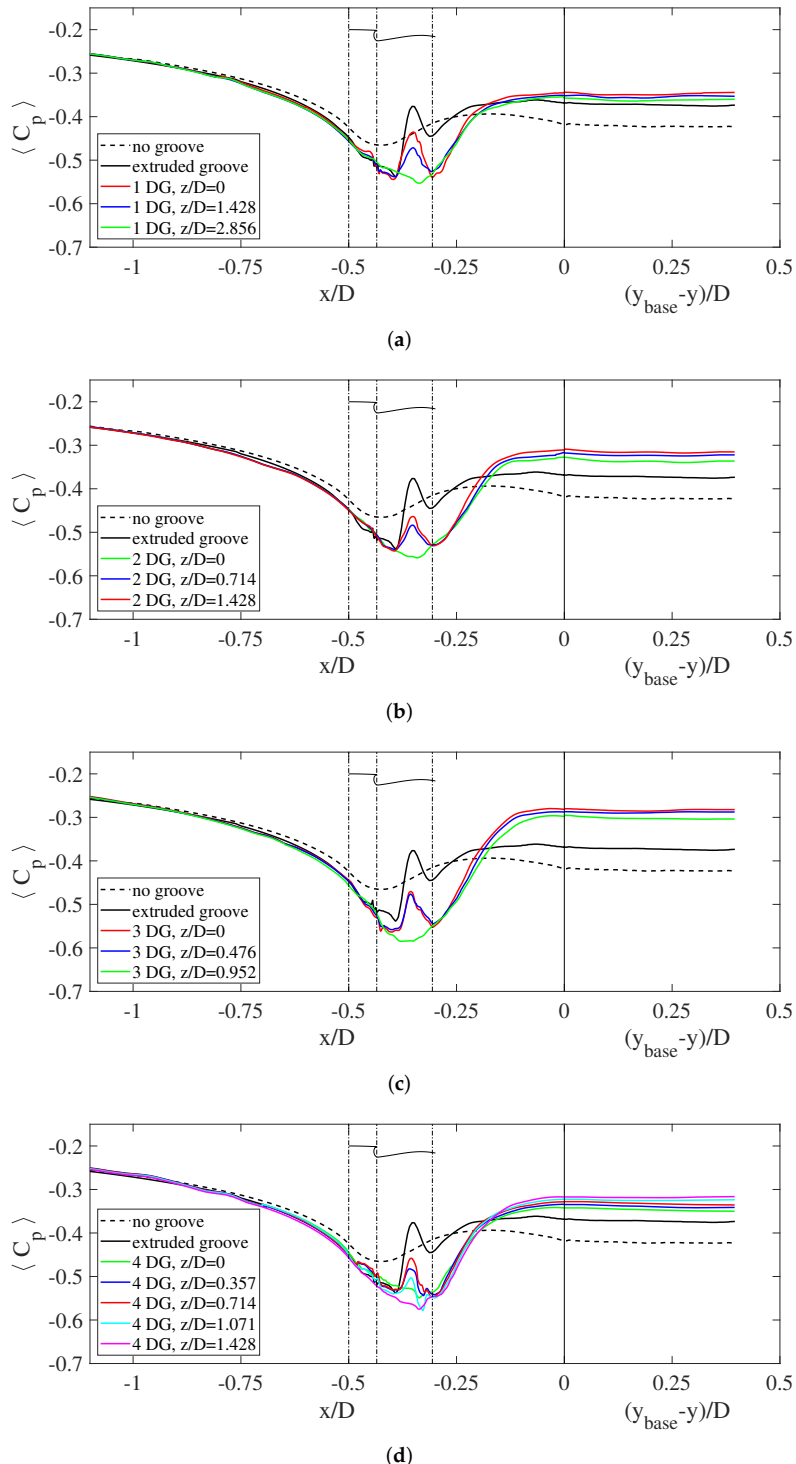


Figure 9. Mean pressure coefficient distributions for the spanwise-discontinuous grooves with: **(a)** $N = 1$, **(b)** $N = 2$, **(c)** $N = 3$, and **(d)** $N = 4$. The results for the boat-tail without the groove and for the extruded groove are from [17].

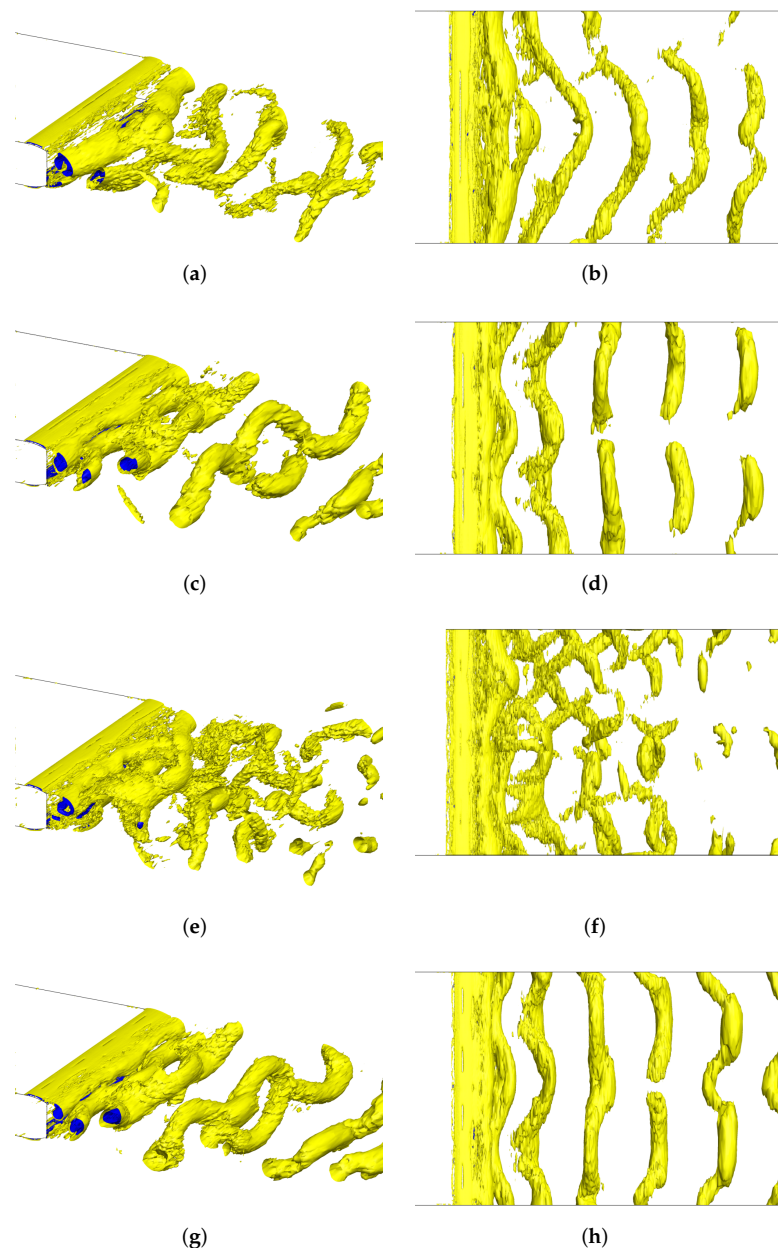


Figure 10. The 3D isometric (left side) and 2D top view (right side) of the instantaneous vortex indicator λ_2 for the spanwise-discontinuous grooves with: (a,b) $N = 1$, (c,d) $N = 2$, (e,f) $N = 3$, and (g,h) $N = 4$.

A quantitative evaluation of the reduction in the vortex-shedding correlation in the spanwise direction is obtained from the computation of the correlation length, L_{corr} . According to [17], the correlation length is computed as follows:

$$L_{corr} = \int_0^{L/D} \rho_u(z) dz = \int_{z/D=0}^{z/D=2.857} \frac{\overline{u(0)u(z)}}{\sigma_u^2} dz \quad (10)$$

where $\rho_u(z)$ is the correlation between the x-velocity signals $u(0)$ and $u(z)$ contemporaneously acquired at $z/D = 0$ and z/D , outside the wake edges 2D downstream of the body, i.e., at $(x/D, y/D) = (2, 0.7)$, and σ_u^2 is their variance. As can be seen from the correlation lengths summarized in Table 3, lower correlation of the velocity signals are found for the spanwise-discontinuous grooves compared with the spanwise-extruded case. For the 3 DG

case, L_{corr} is also below the value for the boat-tail without grooves. No further reduction in the correlation length is present for 4 DG.

Table 3. Correlation lengths for the spanwise-discontinuous grooves and comparison with the plain boat-tail and the boat-tail with spanwise-extruded groove from [17]).

	L_{corr}/D
1 DG	1.53
2 DG	1.39
3 DG	1.23
4 DG	1.42
no groove	1.41
extruded groove	1.96

5. Conclusions

The present study indicates that the introduction of spanwise-discontinuous grooves in the boat-tail lateral surface is effective in delaying separation and in reducing drag, although the grooves occupy a reduced portion of the boat-tail compared with the case of a single spanwise-extruded groove. The maximum reduction in the boat-tail drag is 25.7% in comparison with the boat-tail without grooves and 17.7% with the case of the spanwise-extruded groove. In comparison with a spanwise-extruded groove having the same streamwise section, discontinuous grooves lead to the formation of vortical structures having waves in the spanwise direction and to a consequent reduction in the vortex-shedding correlation. This is probably related to the less-straight flow mean separation line, which, conversely, is perfectly rectilinear for spanwise-extruded grooves.

A systematic analysis is carried out on the effect of the parameter N , being the number of grooves that are present in spanwise direction for N equally-long portions of the total spanwise length of the boat-tail. Increasing N produces an improvement of the flow-control device performance, whose maximum effect is reached for $N = 3$, corresponding to a spanwise extension of the groove, m , roughly equal to the body crossflow dimension, D . Above this value, no further improvements are found. This suggests that there is a minimum value of the groove spanwise length below which no further decrease in the vortex-shedding correlation in the spanwise direction occurs. This is related to vortex-shedding properties and represents an intrinsic limitation of this strategy. For $N > 3$ couples of two neighbors spanwise-discontinuous groove starts to work together and, in practice, four grooves work as they were two longer ones, as confirmed by the results obtained for 4 DG and 2 DG cases.

As future work, experiments on spanwise-extruded and spanwise-discontinuous grooves are planned to investigate the effects on drag reduction and vortex-shedding correlation. Moreover, the effect of two or more subsequent grooves along the boat-tail lateral surface will be analyzed through experiments and simulations.

Author Contributions: Conceptualization, A.M. and M.V.S.; Investigation, E.P. and G.L.; Methodology, A.M. and M.V.S.; Validation, E.P. and G.L.; Writing—original draft, E.P. and G.L.; Writing—review and editing, A.M. and M.V.S. All authors have read and agreed to the published version of the manuscript.

Funding: This research received no external funding.

Institutional Review Board Statement: Not applicable.

Informed Consent Statement: Not applicable.

Data Availability Statement: The data presented in this study are available on request from the corresponding author.

Acknowledgments: The authors wish to thank Guido Buresti for his precious suggestions in the development of the grooves as a passive flow control device.

Conflicts of Interest: The authors declare no conflicts of interest.

Abbreviations

1DG	One spanwise-extruded groove, -
2DG	Two spanwise-extruded groove, -
3DG	Three spanwise-extruded groove, -
4DG	Four spanwise-extruded groove, -
$\langle C_p \rangle$	Mean pressure coefficient, -
a	Length of the ellipse parallel to the lateral surface, m
b	Length of the groove, m
C_D^i	Drag coefficient of the i-th portion of the body, -
$C_{D,p}^{base}$	Pressure drag coefficient of the base of the boat tail, -
$C_{D,p}^{bt}$	Pressure drag coefficient of the boat-tail, -
$C_{D,p}^{ls}$	Pressure drag coefficient of the boat-tail lateral surface, -
$C_{D,tot}^{bt}$	Drag coefficient of the boat-tail, -
$C_{D,v}^{bt}$	Viscous drag coefficient of the boat-tail, -
CFL	Courant–Friedrichs–Lowy number, -
C_P	Pressure specific heat, J/kgK
\bar{C}_p	Time-averaged pressure coefficient, -
$\bar{C}_{p,base}$	Time-averaged pressure coefficient on the base of the boat-tail, -
C_S	SGS constant, -
D	Cross-flow dimension of the main body, m
d	Cross-flow dimension of the base of the boat-tail, m
D^i	Drag of the i-th portion of the body, N
e	Total energy per unit mass, m^2/s^2
E	Symmetric part of the velocity gradient, 1/s
f	Vortex-shedding frequency, Hz
h	Depth of the groove, m
H	SGS term, kg/s^3
L	Total streamwise length of the body, m
L_{corr}	Correlation length, m
LRS	Large Resolved Scale, -
m	Spanwise length of the groove, m
M	SGS stress tensor, Pa
N	Number of grooves, -
p	Pressure of the flow, Pa
P	Strain tensor, 1/s
\bar{p}	Time-averaged pressure, Pa
p_∞	Free-stream pressure, Pa
Pr_{SGS}	SGS Prandtl number, -
Q	Symmetric tensor for the definition of λ_2 , 1/s ²
q	Resolved heat vector flux, kg/ss^3
Re	Reynolds number, -
s	Distance between the groove upstream edge and the beginning of the boat-tail, m
S	Resolved strain tensor, 1/s
SGS	Sub-Grid Scale, -
SRS	Small Resolved Scale, -
St	Strouhal number, -
T	Temperature, K
t	Time, s
u	Streamwise velocity, m/s
u_∞	Free-stream velocity, m/s
$u(z)$	Non dimensional streamwise-velocity signal at the spanwise coordinate z, -

VMS-LES	Variational Multi-Scale Large-Eddy Simulations, -
x_{sep}	Streamwise position of the separation point, m
\bar{x}_{sep}	Time-averaged streamwise position of the separation point, m
$\langle x \rangle_{sep}$	Time- and spanwise-averaged streamwise position of the separation point, m
x_{sep}^{max}	Maximum downstream position of the separation point, m
x_{sep}^{min}	Maximum upstream position of the separation point, m
y^+	Wall y plus, -
y_{sep}	Time-averaged crossflow position of the separation point, m
Δ_S	Filter width, m
Δt	Time step, s
Δx	Grid resolution, m
λ_2	Instantaneous vortex indicator, -
μ	Viscosity of air, kg/ms
μ_{SGS}	SGS viscosity, kg/ms
ν	Kinematic viscosity of air, m ² /s
ρ	Density of air, kg/m ³
ρ_u	Correlation coefficient, -
$\sigma(C_D)$	Standard deviation of the drag coefficient, -
$\sigma(C_L)$	Standard deviation of the lift coefficient, -
$\sigma(C_p)$	Standard deviation of the pressure coefficient, -
σ_u	Standard deviation of the signal $u(z)$, -
τ	Vortex-shedding period, s
Ω	Antisymmetric part of the velocity gradient, 1/s

References

1. Gad-el-Hak, M. *Flow Control: Passive, Active, and Reactive Flow Management*; Cambridge University Press: Cambridge, UK, 2000.
2. Choi, H.; Jeon, W.P.; Kim, J. Control of flow over a bluff body. *Annu. Rev. Fluid Mech.* **2008**, *40*, 113–139. [[CrossRef](#)]
3. Mair, W.A. Reduction of base drag by boat-tailed afterbodies in low-speed flow. *Aeronaut. Quart.* **1969**, *20*, 307–320. [[CrossRef](#)]
4. Mariotti, A. Axisymmetric bodies with fixed and free separation: Base-pressure and near-wake fluctuations. *J. Wind Eng. Ind. Aerod.* **2018**, *176*, 21–31. [[CrossRef](#)]
5. Howard, F.G.; Goodman, W.L.; Walsh, M.J. Axisymmetric bluff-body drag reduction using circumferential grooves. In Proceedings of the Applied Aerodynamics Conference, Danvers, MA, USA, 13–15 July 1983.
6. Howard, F.; Goodman, W. Axisymmetric bluff-body drag reduction through geometrical modification. *J. Aircr.* **1985**, *22*, 516–522. [[CrossRef](#)]
7. Selby, G.; Lin, J.; Howard, F. Turbulent flow separation control over a backward-facing ramp via transverse and swept grooves. *ASME J. Fluids Eng.* **1990**, *112*, 238–240. [[CrossRef](#)]
8. Lin, J. Control of Low-Speed Turbulent Separated Flow over a Backward-Facing Ramp. Ph.D. Thesis, Old Dominion University, Norfolk, VA, USA, 1992.
9. Migay, V.K. The Efficiency of a Cross-Ribbed Curvilinear Diffuser. *Energomashinostroenie* **1962**, *1*, 45–46. (English Translation FTD-TT-62-1151)
10. Stull, F.; Velkoff, H. Effect of transverse ribs on pressure recovery in two-dimensional subsonic diffusers. In Proceedings of the 8th Joint Propulsion Specialist Conference, New Orleans, LA, USA, 29 November–1 December 1972.
11. Jones, E.M. An Experimental Study of Flow Separation over a Flat Plate With 2D Transverse Grooves. Master’s Thesis, University of Alabama, Tuscaloosa, AL, USA, 2013.
12. Lang, A.W.; Jones, E.M.; Afroz, F. Separation control over a grooved surface inspired by dolphin skin. *Bioinspir. Biomim.* **2017**, *12*, 026005. [[CrossRef](#)]
13. Mariotti, A.; Grozescu, A.N.; Buresti, G.; Salvetti, M.V. Separation control and efficiency improvement in a 2D diffuser by means of contoured cavities. *Eur. J. Mech. B-Fluid* **2013**, *41*, 138–149. [[CrossRef](#)]
14. Mariotti, A.; Buresti, G.; Salvetti, M.V. Control of the turbulent flow in a plane diffuser through optimized contoured cavities. *Eur. J. Mech. B-Fluid* **2014**, *48*, 254–265. [[CrossRef](#)]
15. Mariotti, A.; Buresti, G.; Salvetti, M.V. Use of multiple local recirculations to increase the efficiency in diffusers. *Eur. J. Mech. B-Fluid* **2015**, *50*, 27–37. [[CrossRef](#)]
16. Mariotti, A.; Buresti, G.; Gaggini, G.; Salvetti, M.V. Separation control and drag reduction for boat-tailed axisymmetric bodies through contoured transverse grooves. *J. Fluid Mech.* **2017**, *832*, 514–549. [[CrossRef](#)]
17. Mariotti, A.; Buresti, G.; Salvetti, M.V. Separation delay through contoured transverse grooves on a 2D boat-tailed bluff body: Effects on drag reduction and wake flow features. *Eur. J. Mech. B-Fluid* **2019**, *74*, 351–362. [[CrossRef](#)]
18. Rossiter, J.E. *Wind-Tunnel Experiments on the Flow over Rectangular Cavities at Subsonic and Transonic Speeds*; R&M, No. 3438; Aeronautical Research Council: Swindon, UK, 1964.

19. Rockwell, D.; Naudascher, E. Review—Self-sustaining oscillations of flow past cavities. *J. Fluid Eng.-Tans. ASME* **1978**, *100*, 152–165. [[CrossRef](#)]
20. Gharib, M.; Roshko, A. The effect of flow oscillations on cavity drag. *J. Fluid Mech.* **1987**, *177*, 501–530. [[CrossRef](#)]
21. Margason, R.J. Investigation of the Effect of Two-Dimensional Cavities on Boundary Layers in an Adverse Pressure Gradient. Ph.D. Thesis, Naval Postgraduate School, Monterey, CA, USA, 1996.
22. Colonius, T. An overview of simulation, modeling, and active control of flow/acoustic resonance in open cavities. In Proceedings of the 39th Aerospace Sciences Meeting and Exhibit, Reno, NV, USA, 8–11 January 2001.
23. Rowley, C.; Colonius, T.; Basu, A. On self-sustained oscillations in two-dimensional compressible flow over rectangular cavities. *J. Fluid Mech.* **2002**, *455*, 315–346. [[CrossRef](#)]
24. Ringleb, F. Separation control by trapped vortices. In *Boundary Layer and Flow Control*; Lachmann, G.V., Ed.; Pergamon Press: Oxford, UK, 1961; Volume 1, pp. 265–294.
25. Iollo, A.; Zannetti, L. Trapped vortex optimal control by suction and blowing at the wall. *Eur. J. Mech. B-Fluid* **2001**, *20*, 7–24. [[CrossRef](#)]
26. Tutty, O.; Buffoni, M.; Kerminbekov, R.; Donelli, R.; De Gregorio, F.; Rogers, E. Control of flow with trapped vortices: Theory and experiments. *Int. J. Flow Control* **2013**, *5*, 89–110. [[CrossRef](#)]
27. Heller, H.H.; Bliss, D.B. The Physical Mechanism of Flow Induced Pressure Fluctuations in Cavities and Concepts for their Suppression. In Proceedings of the 2nd Aeroacoustics Conference, Hampton, VA, USA, 24–26 March 1975.
28. Pey, Y.; Chua, L. Effects of trailing wall modifications on cavity wall pressure. *Exp. Therm. Fluid Sci.* **2014**, *57*, 250–260. [[CrossRef](#)]
29. Pey, Y.; Chua, L.; Siauw, W. Effect of trailing edge ramp on cavity flow structures and pressure drag. *Int. J. Heat Fluid Flow* **2014**, *45*, 53–71. [[CrossRef](#)]
30. Sarohia, V. Experimental and Analytical Investigation of Oscillations in Flows over Cavities. Ph.D. Thesis, California Institute of Technology, Pasadena, CA, USA, 1975.
31. Sarohia, V. Experimental investigation of oscillations in flows over shallow cavities. *AIAA J.* **1977**, *15*, 984–991. [[CrossRef](#)]
32. Mariotti, A.; Pasqualetto, E.; Buresti, G.; Salvetti, M.V. Effects of spanwise-discontinuous contoured transverse grooves on flow separation and vortex shedding. In *ERCOFTAC Workshop Direct and Large Eddy Simulation*; ERCOFTAC Series; Springer: Cham, Switzerland, 2020; Volume 27, pp. 97–102.
33. Mariotti, A.; Buresti, G.; Salvetti, M.V. Connection between base drag, separating boundary layer characteristics and wake mean recirculation length of an axisymmetric blunt-based body. *J. Fluid Struct.* **2015**, *55*, 191–203. [[CrossRef](#)]
34. Hughes, T.; Mazzei, L.; Jansen, K. Large-eddy simulation and the variational multiscale method. *Comput. Vis. Sci.* **2000**, *3*, 47–59. [[CrossRef](#)]
35. Hughes, T.; Oberai, A.; Mazzei, L. Large-eddy simulation of turbulent channel flows by the variational multiscale method. *Fluids* **2001**, *13*, 1784–1799. [[CrossRef](#)]
36. Germano, M.; Piomelli, U.; Moin, P.; Cabot, W. A dynamic subgrid-scale eddy viscosity model. *Phys. Fluids Fluid Dyn.* **1991**, *3*, 1760–1765. [[CrossRef](#)]
37. Meneveau, C.; Katz, J. Scale invariance and turbulence models for large-eddy simulation. *Ann. Rev. Fluids Mech.* **2000**, *32*, 1–31. [[CrossRef](#)]
38. Koobus, B.; Farhat, C. A variational multiscale method for the large eddy simulation of compressible turbulent flows on unstructured meshes—Application to vortex shedding. *Comput. Methods Appl. Mech. Eng.* **2004**, *193*, 1367–1383. [[CrossRef](#)]
39. Momeau, C.; Mortazavi, I. A review of vortex method and their applications: From creation to recent advances. *Fluids* **2021**, *6*, 68. [[CrossRef](#)]
40. Alcântara Pereira, L.; Oliveira, M.; Moraes, P.; Bimbato, A. Numerical experiments of the flow around a bluff body with and without roughness model near a moving wall. *J. Braz. Soc. Mech. Sci. Eng.* **2020**, *42*, 129. [[CrossRef](#)]
41. Camarri, S.; Salvetti, M.V.; Koobus, B.; Dervieux, A. Large-eddy simulation of a bluff-body flow on unstructured grids. *Int. J. Numer. Methods Fluids* **2002**, *40*, 1431–1460. [[CrossRef](#)]
42. Smagorinsky, J. General circulation experiments with the primitive equations. *Mon. Weather Rev.* **1963**, *91*, 99–164. [[CrossRef](#)]
43. Camarri, S.; Salvetti, M.V.; Koobus, B.; Dervieux, A. A low-diffusion MUSCL scheme for LES on unstructured grids. *Comput. Fluids* **2004**, *33*, 1101–1129. [[CrossRef](#)]
44. Ouvrard, H.; Koobus, B.; Dervieux, A.; Salvetti, M.V. Classical and variational multiscale LES of the flow around a circular cylinder on unstructured grids. *Comp. Fluids* **2010**, *39*, 1083–1094. [[CrossRef](#)]
45. Rocchio, B.; Mariotti, A.; Salvetti, M.V. Flow around a 5:1 rectangular cylinder: Effects of upstream-edge rounding. *J. Wind Eng. Ind. Aerod.* **2020**, *204*, 104237. [[CrossRef](#)]
46. Lunghi, G.; Pasqualetto, E.; Rocchio, B.; Mariotti, A.; Salvetti, M.V. Impact of the lateral mean recirculation characteristics on the near wake and bulk quantities of the BARC configuration. *Wind Struct.* **2022**, *34*, 115–125.
47. Bearman, P.W. On vortex street wakes. *J. Fluid Mech.* **1967**, *28*, 625–641. [[CrossRef](#)]
48. Jeong, J.; Hussain, F. On the identification of a vortex. *J. Fluid Mech.* **1995**, *285*, 69–94. [[CrossRef](#)]